

A MULTISTAGE MULTIGRID METHOD FOR THE
COMPRESSIBLE NAVIER STOKES EQUATIONS

F. Grasso

Ist. di Gasdinamica, P.le Tecchio 80, Napoli, Italy 80125

A. Jameson, L. Martinelli

Dept. of Mech. and Aero. Eng., Princeton N.J., 08544

SUMMARY

Transonic and supersonic laminar flows around a NACA0012 airfoil are computed for different values of the Reynolds number and angle of attack by means of a three-stage explicit finite volume method. Convergence is enhanced by use of multigrid and local time stepping. However the latter is not employed when the flow presents a transient character as is the case of the transonic test case at Reynolds number equal to 10000. Computations have been performed on (256x64) grid. For some cases both (256x64) and (128x32) meshes are employed and the need of high grid resolution in the presence of disparate characteristic length scales is shown. The method is found to be very accurate and robust by comparison of the computed results with experimental data and other numerical results.

INTRODUCTION

The present paper deals with the development of an accurate and robust explicit finite volume method for the solution of viscous transonic flows around airfoils.

Several implicit or semi-implicit algorithms for the solution of the compressible Navier Stokes equations [1]-[3] have been presented within the last decade. In the recent years there has been a growing interest in explicit methods on account of the rapid progress in high speed computers, as well as in the development of efficient Euler solvers [4]-[5]. Several explicit Navier Stokes solvers have appeared [6]-[8]. The present paper is a companion paper of Ref. [8]. In the latter the method has been tested for a variety of transonic flow situations, either laminar or turbulent, and for very large Reynolds numbers. In the present work the method has been tested and validated for a variety of Reynolds numbers, ranging from 73 to 10000, for values of the Mach number in the range $M = .8-2$, and for different values of the angle of attack (α).

The governing equations are discretized by a finite volume technique.

Time integration is performed by using a three-stage Runge Kutta algorithm, together with multigrid to accelerate the evolution of the solution. The computational efficiency of the method is increased by an implicit smoothing of the residuals together with local time stepping. The latter is not employed in the high Reynolds number case that shows a transient character.

In Ref. [8] it is shown that a cell centered formulation (i.e. variables defined at cell centers) is best suited for Neumann type boundary conditions, while a corner point formulation (i.e. variables defined at grid nodes) is more adequate with Dirichlet-type b.c.. The test cases here computed require that the temperature be specified at the wall, and consequently a corner point formulation is used.

The computations have been performed on a scalar computer. However the algorithm is fully vectorizable and should be able to exploit the characteristics of parallel machines.

In the next sections the governing equations are presented and the numerical algorithm is discussed. Finally the results of laminar flows over a NACA0012 airfoil are presented and some concluding remarks given.

GOVERNING EQUATIONS

A dimensionless conservation form of the Navier Stokes equations is used with the following definition of the non-dimensional variables

$$(x^*, y^*) = (x/c; y/c), \text{ where } c \text{ is the chord}$$

$$t^* = t(p_\infty/\rho_\infty)^{1/2}/c$$

$$\rho^* = \rho/\rho_\infty$$

$$u^* = u/(p_\infty/\rho_\infty)^{1/2}$$

$$v^* = v/(p_\infty/\rho_\infty)^{1/2}$$

$$E^* = E/(p_\infty/\rho_\infty)$$

$$p^* = p/p_\infty$$

$$\mu^* = \gamma^{1/2} M_\infty / \text{Re } \mu/\mu_\infty$$

$$\lambda^* = c_p \mu^* / \text{Pr} ,$$

Dropping the * for the sake of brevity, the integral form of the equations is

$$\frac{\partial}{\partial t} \int_V W dV = - \oint_{\partial V} (f n_x + g n_y) dS + \int_V \left(\frac{\partial P}{\partial x} + \frac{\partial Q}{\partial y} \right) dV \quad (1)$$

where W , $f(g)$ and $P(Q)$ are respectively the vector unknown, the non dissipative and the viscous flux components in $x(y)$, and they are given by:

$$W = [\rho, \rho u, \rho v, \rho E]^T$$

$$f = [\rho u, \rho u^2 + p, \rho uv, \rho u(E + p/\rho)]^T$$

$$g = [\rho v, \rho vu, \rho v^2 + p, \rho v(E + p/\rho)]^T$$

$$P = [0, \sigma_{xx}, \sigma_{xy}, u\sigma_{xx} + v\sigma_{xy} - q_x]^T$$

$$Q = [0, \sigma_{xy}, \sigma_{yy}, u\sigma_{xy} + v\sigma_{yy} - q_y]^T$$

where

$$\sigma = \mu [(\nabla u + \nabla u^T) - \frac{2}{3} \nabla \cdot u \underline{I}]$$

$$q = - \frac{\gamma}{Pr} \mu \nabla e .$$

The pressure p is obtained from the equation of state:

$$p = \rho e = (\gamma - 1) [E - (u^2 + v^2)/2] .$$

The Chapman-Rubesin approximation is employed to evaluate the viscosity coefficient.

NUMERICAL SOLUTION

The computational domain is divided into arbitrary quadrilateral cells. The system of governing equations is reduced to a system of ordinary differential equations (ODE) by using the method of lines to decouple the spatial and temporal terms. Use of mean value theorem and mid-point rule (to evaluate the volume and surface integrals) yield the following ODE:

$$\frac{d}{dt} (WV) = -C + D + AD \quad (2)$$

where V , C , D and AD are respectively the sum of the volumes of the four cells surrounding node ij , the net inviscid, dissipative and adaptive dissipation contributions.

A corner point formulation is employed to accurately satisfy the boundary conditions of Dirichlet-type required by the test cases. The net inviscid contribution at each node ij is obtained as the sum of the net contributions over the four surrounding cells so as to increase the computational efficiency and to guarantee conservation. The following expression is obtained:

$$C_w = \sum_{c=1,4} \left(\sum_{k_c=1,4} [(\hat{f}_n + \hat{g}_n) \Delta S]_{k_c} \right) \quad (3)$$

where c is the index of the (four) cells surrounding node ij , and k_c is the face index of cell c .

The numerical flux (\hat{f}, \hat{g}) at cell face k_c is computed as the average of the corresponding values at the two adjacent cells. Such a procedure is computationally efficient and it yields second order accuracy on a smooth grid.

Gauss theorem is used first to evaluate the numerical diffusion flux components (\hat{P}, \hat{Q}) at cell centers and then to compute their divergence at node ij . For example, the net contribution for the x -momentum component is [8]:

$$D_{\rho u} = \{ [(\hat{\sigma}_{xx_1} - \hat{\sigma}_{xx_3})(y_{c_2} - y_{c_4}) - (\hat{\sigma}_{xx_2} - \hat{\sigma}_{xx_4})(y_{c_1} - y_{c_3})] + \\ - [(\hat{\sigma}_{xy_1} - \hat{\sigma}_{xy_3})(x_{c_2} - x_{c_4}) - (\hat{\sigma}_{xy_2} - \hat{\sigma}_{xy_4})(x_{c_1} - x_{c_3})] \} / \\ [(x_{c_1} - x_{c_3})(y_{c_2} - y_{c_4}) - (x_{c_2} - x_{c_4})(y_{c_1} - y_{c_3})] \quad (4)$$

where $\hat{\sigma}$ and x_c (y_c) are respectively the discretized stress tensor, and $x(y)$ coordinate of the center of cell c .

The adaptive dissipation (AD_w) , as designed in Ref. [9], is still added to the scheme to inhibit even/odd mesh points decoupling, and to prevent non linear 10^{-3} instabilities. However the amount of artificial dissipation added is 10^{-3} times smaller than the physical one.

ODE is integrated in time by using a three-stage Runge Kutta scheme that guarantees damping of high frequency modes. The physical and adaptive dissipative contributions are evaluated at the first stage in terms of the solution at time level n , and are not reevaluated at each stage.

The solution is advanced in time as follows

$$w^{(0)} = w^n \\ w^{(k)} = w^{(0)} - \alpha_k \frac{\Delta t}{V} [C_w^{(k-1)} - D_w^{(0)} V - AD_w^{(0)}] \\ w^{n+1} = w^{(3)} \quad (3)$$

where $\alpha_1 = \alpha_2 = .6$; $\alpha_3 = 1$.

The efficiency of the method is increased by advancing the solution at each computational cell at its own Δt , so that any disturbance propagates out of the field at a rate proportional to the number of points in the outward direction. Use of such local time stepping fails when the solution presents a transient character, as in case 6 of Table 1 corresponding to $M = .85$, $Re = 10000$, $\alpha = 0^\circ$. The vortices that form at the trailing edge are responsible for the unsteady behaviour, and the solution is advanced in time with a time step corresponding to the most critical stability restriction. Implicit smoothing of the residuals is also used to increase the region of stability, yielding a higher CFL limit [9].

The multigrid strategy devised by Jameson for the solution of the Euler

equations, and extended to the Navier Stokes equations by these authors [8], has also been used in the present work. Auxiliary meshes are introduced by doubling the mesh spacing. The coarser grid variables are initialized so as to conserve mass, momentum and energy. The multistage scheme is reformulated with the results that the solution on a coarse grid is driven by the residuals collected on the next finer grid [8], [9]. The process is repeated on successively coarser grids. After reaching the coarsest grid, the corrections are passed back to the next finer grid by bilinear interpolation.

Boundary conditions

At the wall the following boundary conditions are imposed:

$$u = v = 0$$

$$T_w = T_\infty \left(1 + \frac{\gamma-1}{2} M_\infty^2 \right).$$

The pressure is obtained from the equation of state:

$$p_w = \rho_w T_w$$

where ρ_w is computed from mass conservation.

The far field boundary is located 18 chords away from the airfoil, and conditions, based on the introduction of Riemann invariants for a one dimensional flow normal to the boundary, are employed.

Mesh description

The mesh used in the computations is a body fitted C-mesh obtained by using a hyperbolic grid generator, kindly provided by L. Wigton of the Boeing Co. The computational domain is discretized in 256x64 cells on the finer mesh, however for some test cases computations have also been performed on a coarser grid (128x32). The first point in the boundary layer is located at .002 chords away from the wall, and 5/8 of the total number of points in the streamwise direction are fitted on the airfoil.

RESULTS AND DISCUSSION

Transonic and supersonic laminar flows around NACA0012 airfoils have been computed for different values of the Reynolds number and angle of attack. All the calculations have been carried out on a IBM 3081 scalar machine; the CPU time for a typical run on a 256x64 grid (see Fig. 1) with

three levels of multigrid (and 500 multigrid cycles) is 149 minutes.

For most of the cases convergence is quite satisfactory. The steady state is reached within 300-500 (multigrid) cycles and the RMS of density residual reduces to $0(10^{-3}-10^{-4})$.

When assessing the validity of a computational tool, in the absence of analytical results, it is extremely important to compare the computed results with available experimental data and/or computed results. Figs. 2-3 show a comparison of the computed density with the experimental one of Ref. [10], corresponding to cases 1 and 3 of Table 1. One observes that overall the agreement is rather satisfactory. In both cases there are some disagreements at the trailing edge. However the results shown correspond to rather large values of the RMS of density residuals. Note that in the supersonic case the location and thickness of the detached bow shock is very well predicted.

The robustness of the method and its accuracy is also shown by the comparison of the results for the other cases with those obtained by the others. The computed results show the capability of the method to accurately predict transonic and supersonic flows at different Reynolds numbers ranging from very low to high values (Figs. 4-23). Some discrepancies in the level of the predicted skin friction coefficient are observed, most likely on account of the Chapman-Rubesin approximation employed to evaluate the viscosity coefficient.

Case 6 of Table 1 is the most interesting and critical test case. At $M = .85$, $Re=10000$ and $\alpha = 0^\circ$ an unsteady behaviour of the flow is observed and vortices are shed from the trailing edge as shown in Figs. 26-27. On account of the transient character, local time stepping is not employed and a time step corresponding to the most critical stability restriction is used. A non symmetric field is obtained ($c_L=.1386$, $c_D=.0723$) and no convergence is achieved. Figs. 28-31 show the results for the same case obtained on an intermediate grid (128x32). When computing on such a grid no vortices form. Moreover a pseudo-convergence is reached, and a symmetric solution is obtained ($c_L=.0$, $c_D=.046$) with a value of the RMS of density residual equal to -2.59.

The two completely different results, obtained when using two different mesh refinements, indicate that higher temporal and spatial accuracies are required in the presence of disparate length and time scales. Under these circumstances the local time stepping technique cannot be used and highly refined grids must be employed or else adaptive mesh enrichment should be used [11]-[13] to accurately detect small scale structures.

REFERENCES

- [1] Steger J.L., "Implicit Finite Difference Simulation of Flow About Arbitrary Geometries with Applications to Airfoils," AIAA paper no. 77-665, 1977.
- [2] Beam, R. and Warming, R., "An implicit Factored Scheme for the Compressible Navier-Stokes Equations," AIAA J. Vol. 16, 1978.
- [3] Barth, J., Pulliam, T. and Bunning, P., "Navier Stokes Computations for Exotic Airfoils," AIAA paper no. 85-0109, 1985.
- [4] Jameson, A., Schmidt, W. and Turkel, E., "Numerical Solutions of the Euler Equations by Finite Volume Methods Using Runge-Kutta Time-Stepping Schemes," AIAA paper no. 81-1259, 1981.
- [5] Jameson, A., Baker, J. and Weatherhill, N., "Calculation of the Inviscid Transonic Flow over a Complete Aircraft," AIAA paper no. 86-0103, 1986.
- [6] Agarwaal, R. and Deese, L., "Computations of Transonic Viscous Airfoil, Inlet and Wing Flowfields," AIAA paper no. 84-1551, 1984.
- [7] Swanson, R.C. and Turkel, E., "A Multistage Time-Stepping Scheme for the Navier Stokes Equations," AIAA paper no. 85-0035, 1985.
- [8] Martinelli, L., Jameson, A. and Grasso, F., "A Multigrid Method for the Navier Stokes-Equations," AIAA paper no. 86-0208, 1986.
- [9] Jameson, A., "Transonic Flow Calculations," MAE Report no. 1651, Princeton University, 1983.
- [10] Allegre, J., Lengrand, J.C. and Raffin, M., "Champs d'Ecoulements Rarefiée Compressibles Autour d'un Profil," SESSIA Rep. 894/82.380, 1982.
- [11] Berger, M. and Jameson, A., 9th ICNMFD, Saclay, France, 1985.
- [12] Dannenhoffer, J.F. and Baron, J.R., "Grid Adaptation for the 2-D Euler Equations," AIAA paper no. 85-0484, 1985.
- [13] Bassi, F., Grasso, F. and Savini, M., 10th ICNMFD, Beijing, China, 1986.

ACKNOWLEDGEMENT

The authors wish to thank Drs. B. Mantel and J. Periaux of AMD-BA for their help in plotting the results.

Table 1 - Integral Values of Computed Test Cases

Case	Grid Points	M_∞	Re	α	c_L	c_D	$\log(dp/dt)$
1	256x64	.8	73	10°	.6657	.2522	-2.34
2	256x64	.8	500	10°	.4797	.1597	-3.50
3	256x64	2.0	106	10°	.3716	.1851	-1.74
4	256x64	.85	500	0°	.0	.0964	-3.75
5	256x64	.85	2000	0°	.0	.068	-3.62
6.1	128x32	.85	10000	0°	.0	.046	-2.59
6.2	256x64				.1386	.0723	-0.10

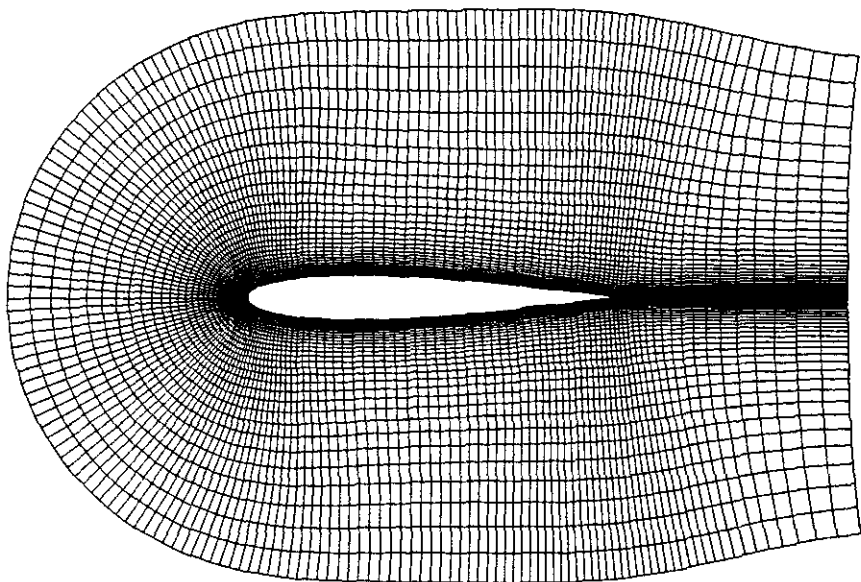


Fig. 1 Computational Grid

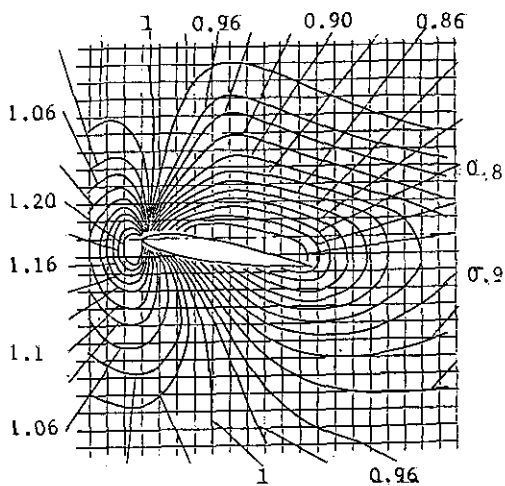


Fig. 2.a - Experimental Density
Contours

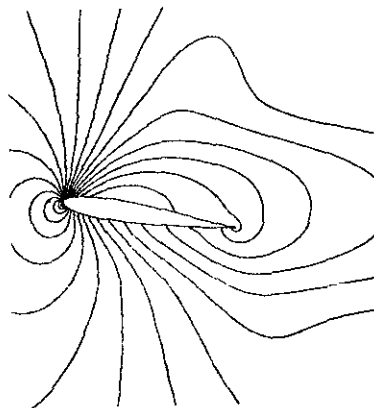


Fig. 2.b - Computed Density
Contours (DR = .05)

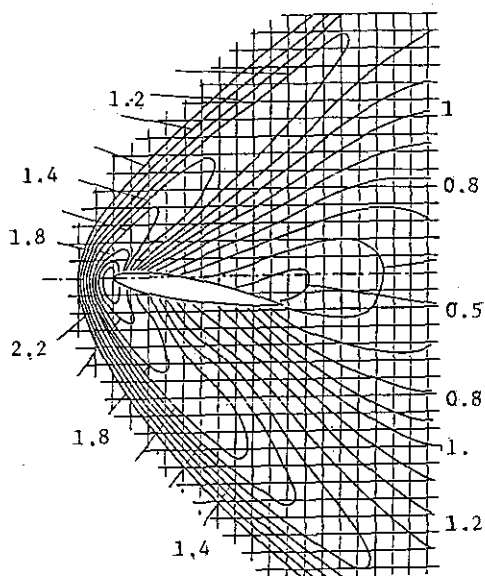


Fig. 3.a - Experimental Density
Contours

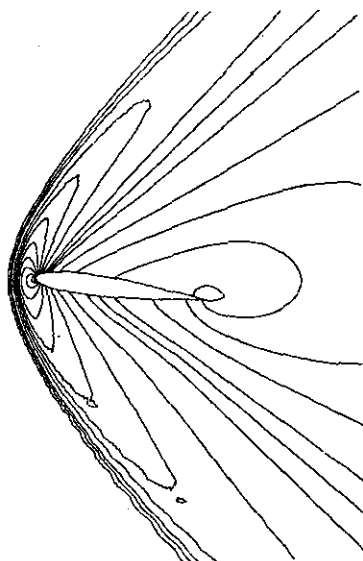


Fig. 3.b - Computed Density
Contours (DR = .2)

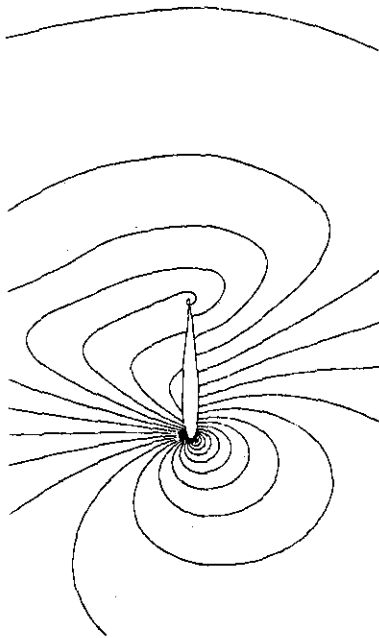


Fig. 4 - Pressure Contours (DP = .05)

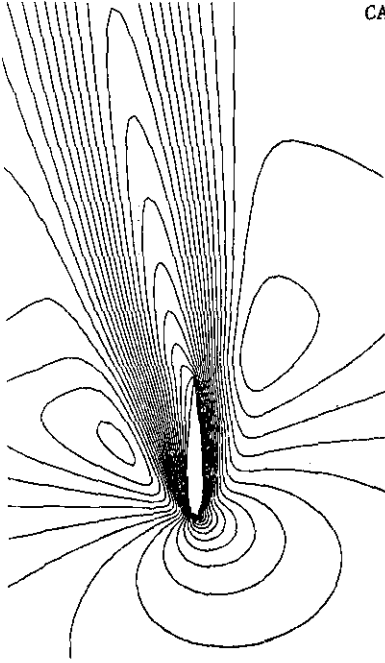


Fig. 5 - Mach Contours (DM = .05)

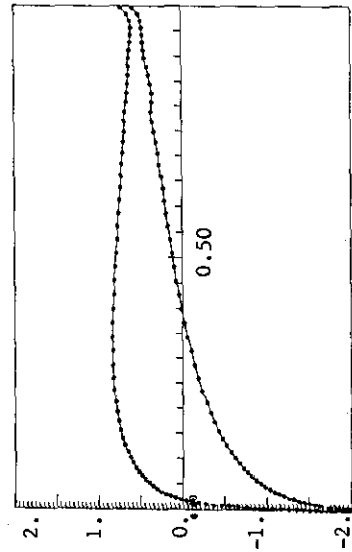


Fig. 6 - Pressure Coefficient vs x

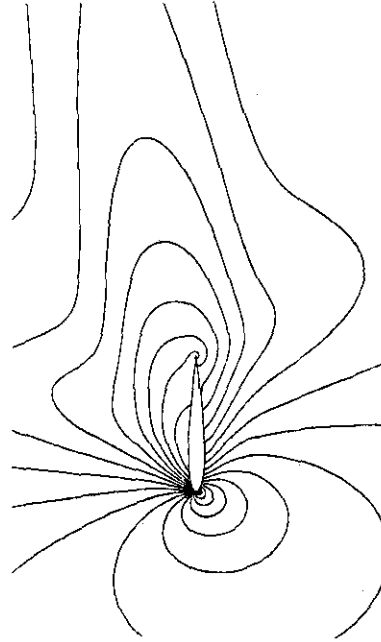


Fig. 7 - Density Contours (DR = .05)

CASE 1 (256x64)

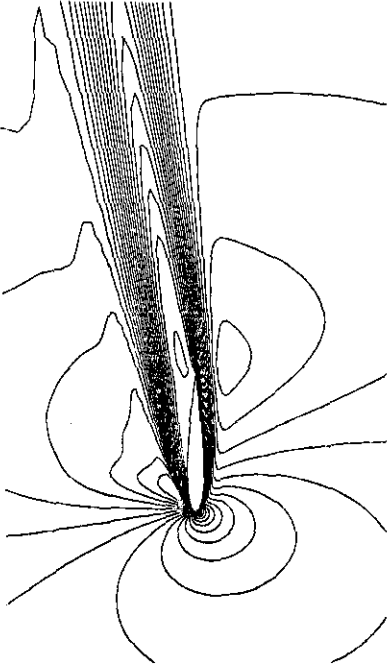


Fig. 9 - Mach Contours (DM = .05)

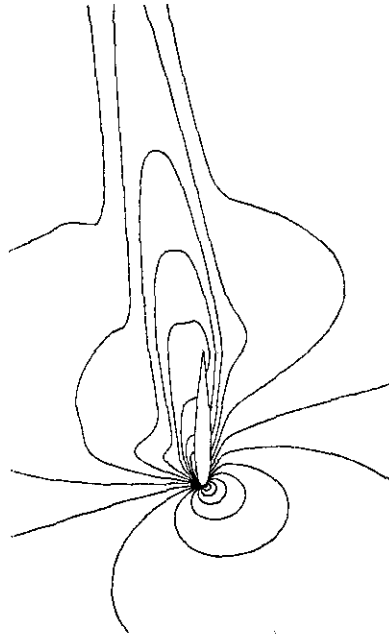


Fig. 11 - Density Contours (DR = .05)

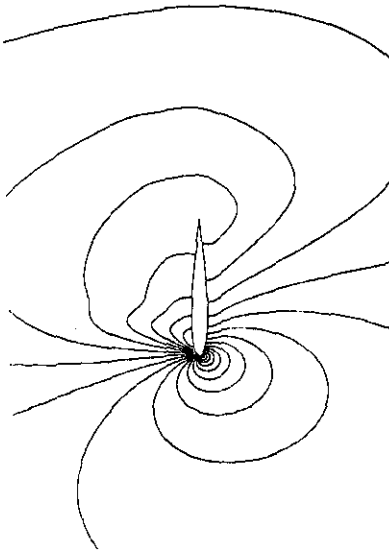


Fig. 8 - Pressure Contours (DP = .05)

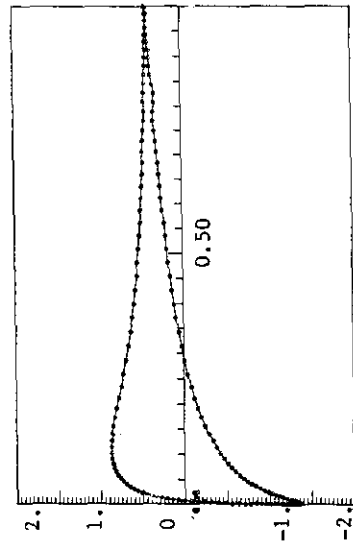


Fig. 10 - Pressure Coefficient vs x

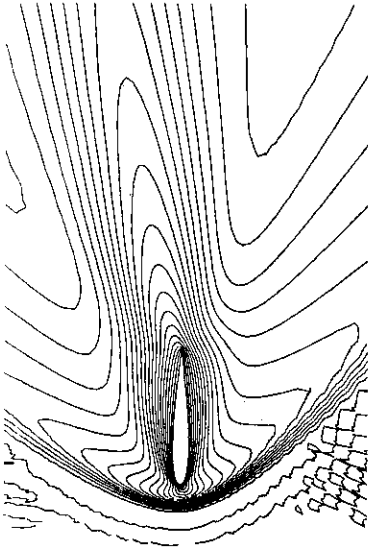


Fig. 13 - Mach Contours (DM = .10)

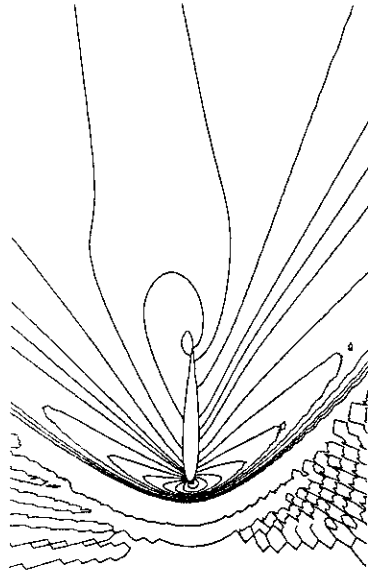


Fig. 15 - Density Contours (DR = .10)

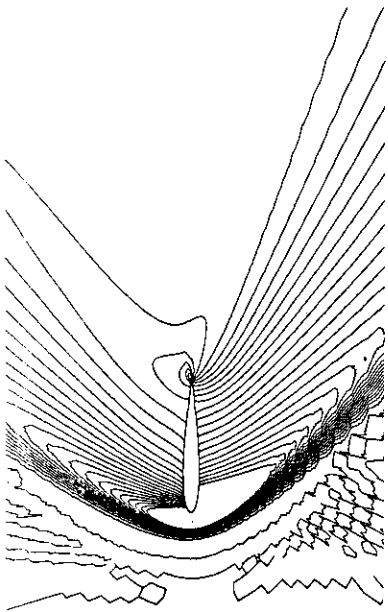


Fig. 12 - Pressure Contours (DP = .10)

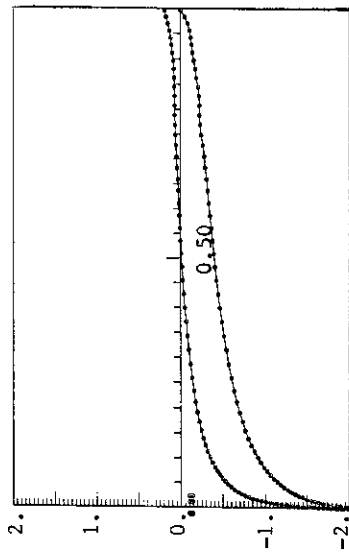


Fig. 14 - Pressure Coefficient vs x

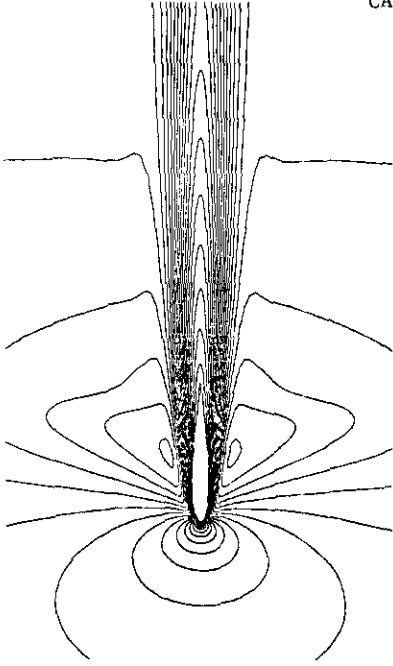


Fig. 17 - Mach Contours (DM = .05)

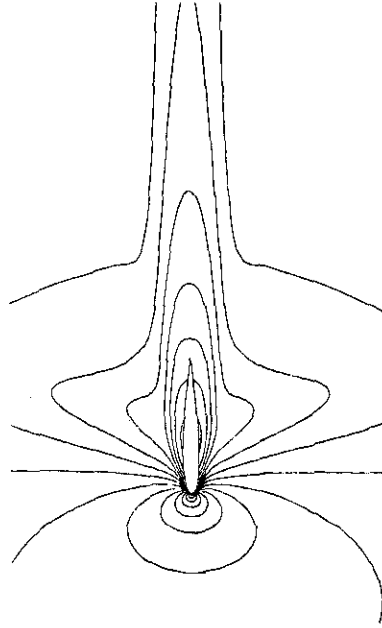


Fig. 19 - Density Contours (DR = .05)

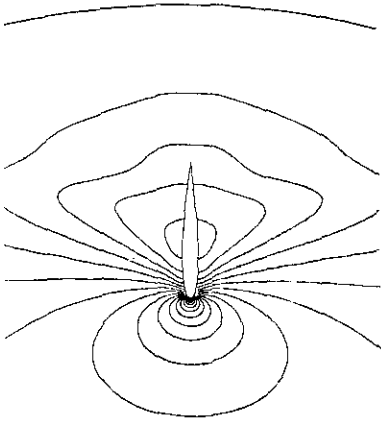


Fig. 16 - Pressure Contours (DP = .05)

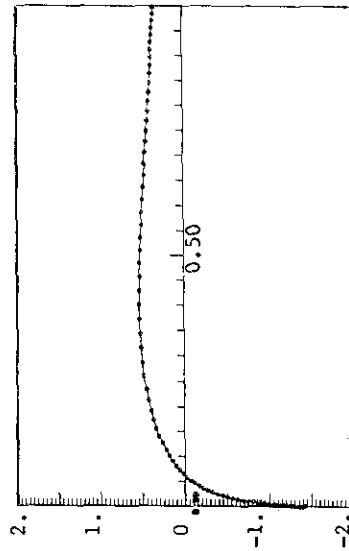


Fig. 18 - Pressure Coefficient vs x

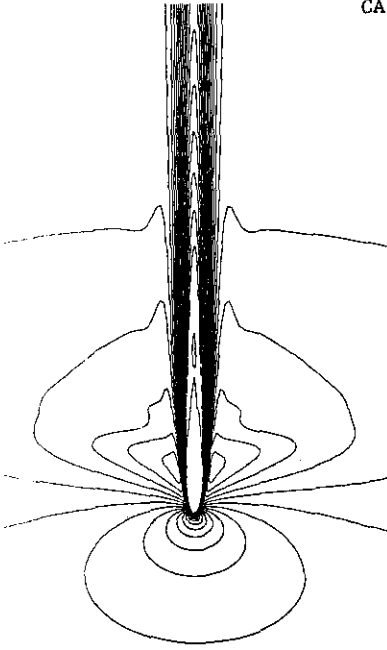


Fig. 21 - Mach Contours (DM = .05)

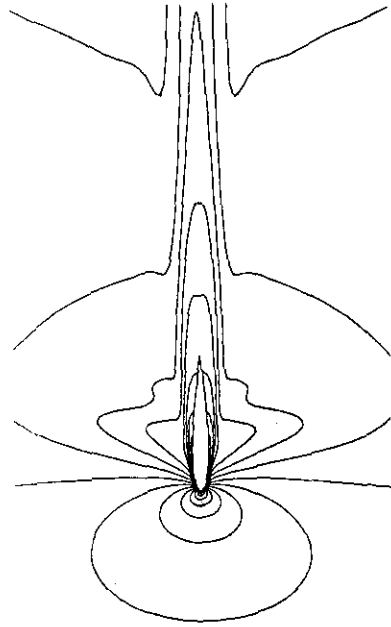


Fig. 23 - Density Contours (DR = .05)

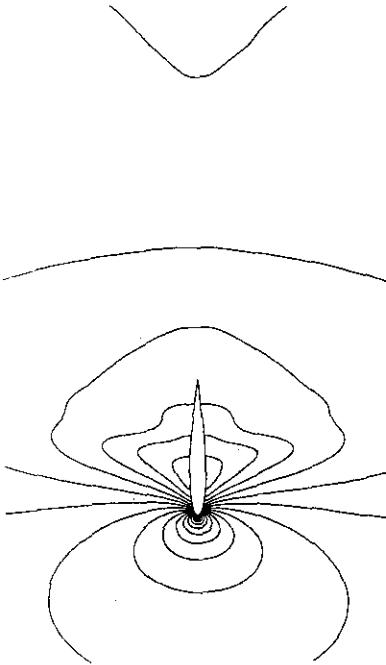


Fig. 20 - Pressure Contours (DP = .05)

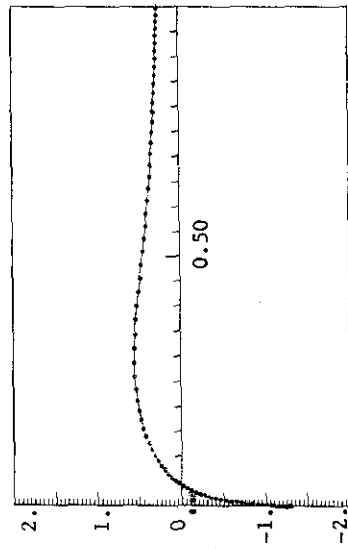


Fig. 22 - Pressure Coefficient vs x

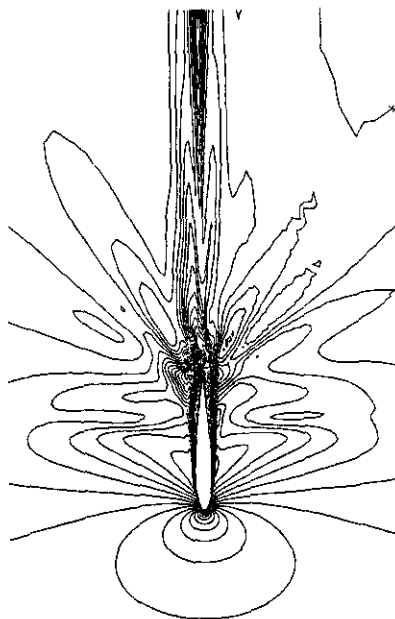


Fig. 25 - Mach Contours (DM = .05)

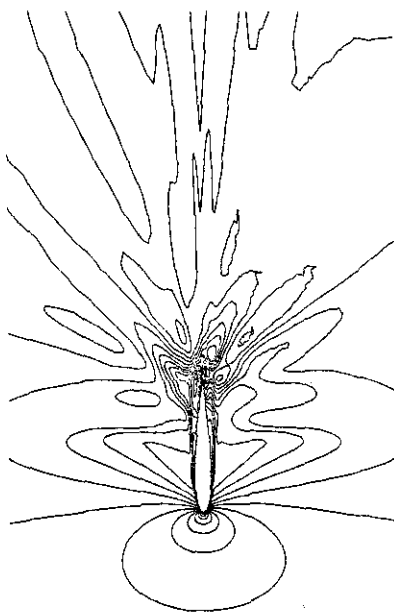


Fig. 27 - Density Contours (DR = .05)

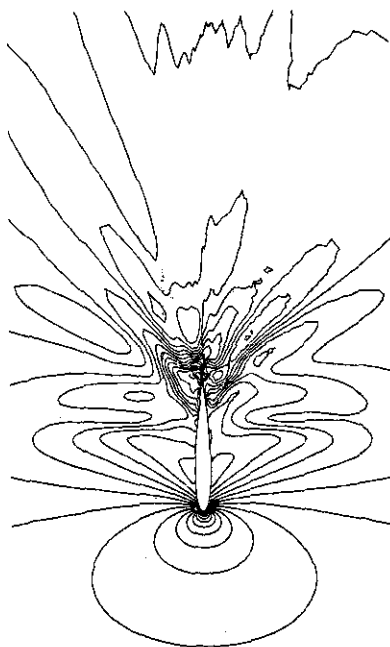


Fig. 24 - Pressure Contours (DP = .05)

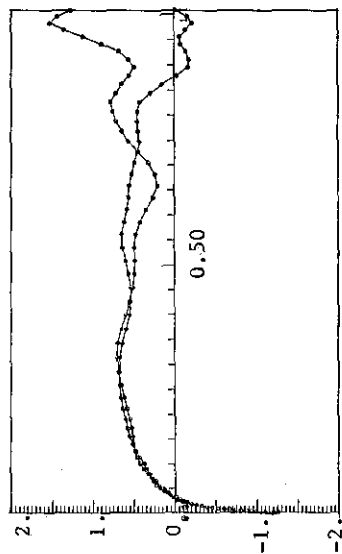


Fig. 26 - Pressure Coefficient vs x

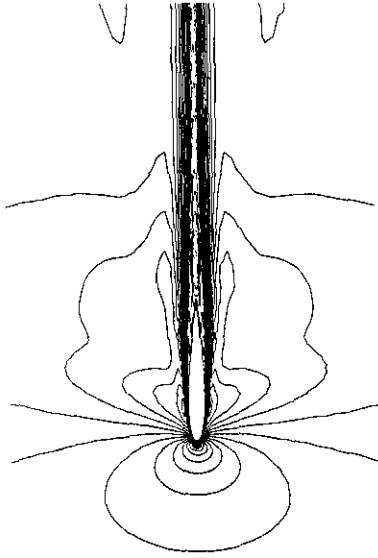


Fig. 29 - Mach Contours (DM = .05)

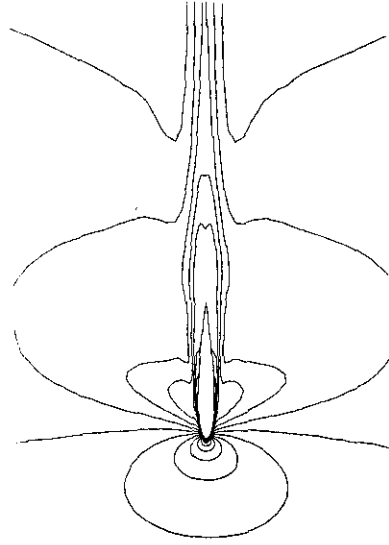


Fig. 31 - Density Contours (DR = .05)

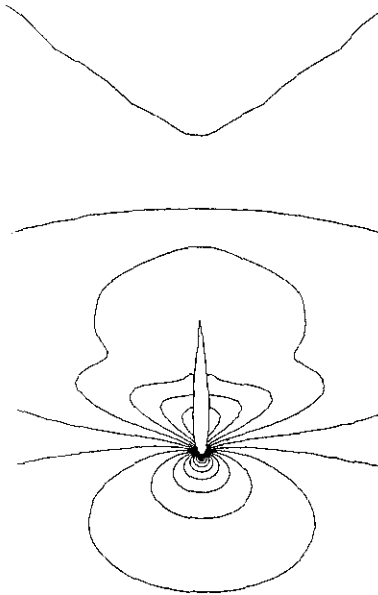


Fig. 28 - Pressure Contours (DP = .05)

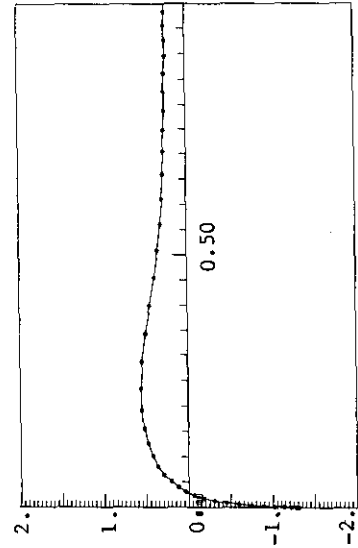


Fig. 30 - Pressure Coefficient vs x